A 3D automatic mesh refinement X-FEM approach for fatigue crack propagation

Gaël Gibert, Benoit Prabel, Anthony Gravouil, Clémentine Jacquemoud

Version of Record: https://www.sciencedirect.com/science/article/pii/S0168874X18306632
Manuscript_6a2abe70c2791be2a552d6c2e83b47e0

A 3D automatic mesh refinement X-FEM approach for fatigue crack propagation.

Gaël GIBERT[a,b,*], Benoit PRABEL[a], Anthony GRAVOUIL[b], Clémentine JACQUEMOUD[a]

[a] *DEN-Service d'études mécaniques et thermiques (SEMT), CEA, Université Paris-Saclay, F-91191, Gif-sur-Yvette, France*
[b] *Université de Lyon, LaMCoS, INSA-Lyon, CNRS UMR5259, F-69621 Lyon, France*

Abstract

A new approach combining the eXtended Finite Element Method (X-FEM) and automatic Adaptive Mesh Refinement (AMR) is presented taking advantage of both methods. The X-FEM, developed over the past two decades by a large community, have proven its efficiency to handle evolving discontinuities in a variety of fracture analysis. Since this method enables to describe the crack and its propagation independently of the mesh of the structure, a simple hierarchical mesh refinement procedure can be applied. Automatic adaptive remeshing is a valuable method in 3D elastic-plastic crack propagation analysis since it permits a locally fine mesh and then an accurate description of physical quantities in a limited area around the crack front. This is particularly important when local fracture criteria are concerned.Moreover local refinement saves computational effort, which is relevant for engineer-sized problems, particularly when the propagation path is not *a priori* known. In the present work, it is shown that both methods combine with minimal effort: the kinematic continuity relations and the field transfer process, needed for history-dependent material, must include in a proper way the enrichment of the model. If this requirement is not fulfilled, numerical error may be introduced. Implementation of this combined X-FEM/AMR approach is presented in detail. In particular, an innovative field transfer strategy is proposed. Numerical applications in 2 and 3 dimensions of crack propagation in elastic-plastic media demonstrate accuracy, robustness and efficiency of the technique.

Keywords: eXtended Finite Element Method, automatic Adaptive Mesh Refinement, 3D crack propagation, non-Linear behaviour, field transfer

1. Introduction

To guarantee the high level of safety of industrial components under exceptional loadings or fatigue cycles without adding unnecessary wide safety margin, it is essential to be able to predict the initiation and the growth of cracks during the entire life time of components.

Physics of cracks propagation is complex, mainly because it involves mechanisms at different scales. Firstly, the global response of the studied structure to any given thermal or mechanical loading is needed. Secondly, theory of fracture mechanics introduced by Griffith [1] and Irwin [2] (also detailed in a large literature like the books of Lemaitre and Chaboche [3] or Kaninnen and Popelar [4]) demonstrates the existence of a zone where the strain and the stress fields are proportional to $\frac{1}{\sqrt{r}}$, r being the distance to the crack front. The zone where this asymptotic solution is predominant is called K-dominance zone. If the loading is sufficiently small compared to the plasticity threshold, small scale yielding conditions apply and the K-dominance zone is preponderant over the plastic zone (figure 1a). When increasing the loading, plasticity may become non-negligible, and the plastic zone become more important (figure 1b). As showed by Elguedj [5], the energy dissipated in this zone may significantly influence the propagation of the crack. Finally, at an even lower scale, the process zone describes the highly non-linear decohesion process responsible for the failure of the material (e.g. growth and coalescence of micro cavities).

Consequently, an accurate modeling of crack propagation should take into account all these scales of interest. This is why in the context of Finite Element Analysis, automatic adaptive refinement techniques have been widely developed for crack propagation modeling in order to "catch" every significant scales. Referring to the classification proposed by Zienkiewicz *et al* [6, 7], it is possible to distinguish: the h-refinement consisting in resizing elements which are too large or too small for the expected quality, from the p-refinement which introduces higher order shape functions in elected ele-

*Corresponding author
Email address: gael.gibert@cea.fr (Benoit PRABEL)

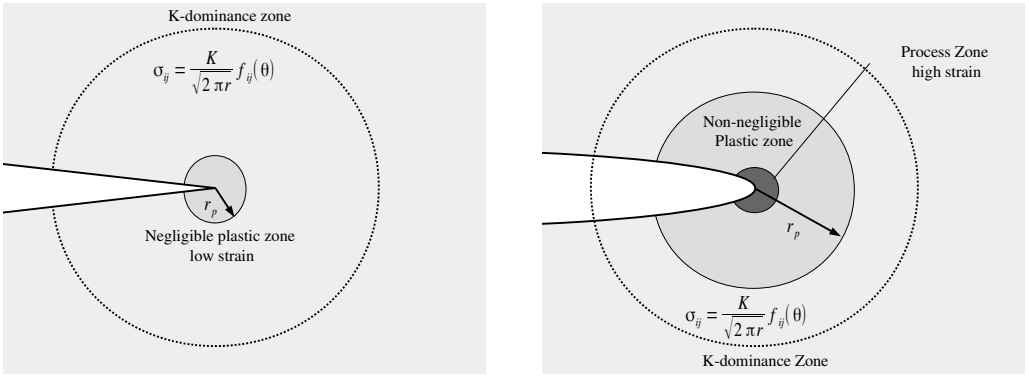

(a) Linear fracture mechanics (b) Elastic-plastic fracture mechanics

Figure 1: Hypothesis of confined plasticity

ments. It is once again possible to split h-refinement into two main variants (but others exist):

(i) the *element subdivision* scheme approach that just splits elected elements (generally as power of 2) tending to preserve their aspect ratio but generally introducing hanging nodes,

(ii) and *remeshing* approaches that locally or globally change the mesh according to a prescribed density.

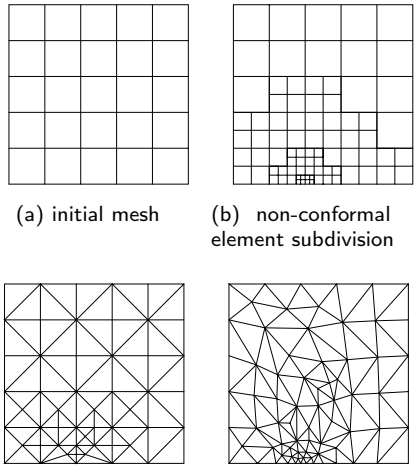

(a) initial mesh (b) non-conformal element subdivision

(c) conformal element subdivision (d) global remeshing

Figure 2: h-refinement

Refinement techniques imply a transfer (also called mapping) from the previous discretization $\mathcal{M}^n$ to the new one $\mathcal{M}^{n+1}$ of the displacement, strain, stress, and internal variables which constitute the state. Practically, some quantities are first transfered to the new discretization and then others are deduced from model considerations in order to reach as good as possible equilibrium, kinematic compatibility, and consistency with the constitutive equation, on a transfered state as close as possible to the one on the previous discretization (conservation of the dissipated energy and minimization of the numerical diffusion for example).

The main difficulty on this step is to transfer variables that are only known at the integration points of the old mesh $\mathcal{M}^1$. Different procedures exist:

(i) This transfer operator can be constructed by taking a constant value over the area associated with every integration points of the old mesh. This was presented for example by Bérard [8].

(ii) The most popular possibility is to construct a continuous approximation of the variable field and then interpolate this approximation at the point where it is needed. Ortiz and Quigley [9] propose this kind of approach using a specific mesh built upon the integrations points themselves, while Peric *et al* [10] use the shapes functions of the finite elements of $\mathcal{M}^n$ in the context of small strain. Lee and Bathe [11] describe a similar approach extended to finite strain elasto-plasticity. Mediavilla *et al* [12] also uses this kind of procedure and shows that it usually requires a balancing step and a recovering of the yield condition afterward.

(iii) A last type of method presented by Brancherie *et al* [13] considers the transfer as a minimization problem and does not rely on the finite element shape functions but on a diffuse approximation. In this approach, equilibrium and constitutive laws can be seen as constrains of the minimization algorithm so balancing and recovering steps can be avoided.

In the general case, the fields transfer from a mesh to another may be a very complex task. This explains

why automatic refinement techniques are often limited to the linear elastic crack propagation simulation.

As detailed in the review [14], the second approach (*remeshing*) is adopted by most numerical softwares like FRANC3D [15] or ADAPCRACK [16] in which remeshing is limited to the vicinity of the crack front (with some submodelling technique). Generally limited to fatigue simulation, an application of this method to dynamic crack propagation can be found in [17]. Chiaruttini *et al* [18] have developed an efficient global remeshing tool (named "Z-crack") to get a very fine mesh for the process zone (with a mesh size about $h = l_c/4$, l_c being the characteristic length of the process zone) in which may lie some cohesive elements enable to dissipate surface energy, and a more coarse mesh for the non-damaged zone close to the process zone (with a prescribed element size of $h = l_c$). Since the non-linearity is concentrated in the cohesive elements, there is no projection of inelastic variable in the bulk. Khoei *et al* [19] use the modified-superconvergent patch recovery for remeshing. Murotani *et al* [20] present an efficient automatic adaptive meshing strategy based on a hierarchical mesh generated by edge collapse and vertex split, and combine it with a p-refinement to avoid too small element size at the crack tip.

The first approach (*subdivision*) is rarely used for crack propagation modeling. Park *et al* [21] combine it with cohesive zone model for dynamic crack propagation modeling and Meyer *et al* [22] use this approach for bi-dimensional fatigue. For both the subdivision of element must be compatible with the crack growth. Except for in-plane crack propagation, the crack surface generally does not intersect the middle of the edge of element, resulting in an arbitrary subdivision. Then more computational effort is required and element may be split into large and tiny subelements. This limitation motivates a coupling with the X-FEM/G-FEM methods. Another promising way of investigation concerns the coupling of subdivision h-refinement with phase-field approach like proposed in [23, 24]

The eXtended Finite Element Method proposed by Belytschko *et al* [25] in 1999 and the Generalized Finite Element Method (G-FEM) proposed by Duarte *et al* [26] in 2000 have been developed over the past two decades by a rather large community ([27, 28, 29, 30, 31, 32, 33, 34]...). X-FEM/G-FEM methods are based on the partition of unity. The bulk structure is meshed disregarding the crack. Specific enriched shapes functions are added to represent the crack opening and the crack tip singularity. As a counterpart, integration of such function may be cumbersome if machine-accuracy is targeted [35, 36], but simplified integration scheme can be used [5, 37]. These methods have been applied successfully to many different industrial fracture mechanics problems. For instance, in the industrial finite element code Cast3m [38] the X-FEM has been used to simulate various cases from the dynamic propagation of a cleavage crack [37, 39] to rolling fatigue involving frictional contact between the cracks lips [40]. Although these methods aim at producing a satisfactory solution for a relatively coarse mesh, accuracy can only be achieved by using a sufficiently fine mesh.

One possibility developed by Rannou [41],[42], and Passieux [43] is to couple the X-FEM method with a multigrid algorithm. This method has proven its efficiency for linear fracture mechanics. However when dealing with non-linear behavior, it rises some non trivial difficulties.

hp-refinement combined with G-FEM is proposed in [44, 45], where the h-refinement is performed using a hierarchical subdivision approach with a conformal meshing between refined and unrefined zones that avoid hanging nodes. In [46] an other conformal automatic h-adaptive mesh refinement strategy is proposed but combined with X-FEM for 3D elastic crack propagation. A straightforward hierarchic refinement algorithm has been successfully coupled with X-FEM by Fries *et al* [47] for 2D elastic non-propagating crack. The case of enriched hanging nodes is discussed. In [48], Prange *et al* also adopt a hierarchic mesh refinement technique for 2D crack problems, but avoid the case of enriched hanging nodes. They use the Zienkiewicz and Zhu error estimator because more adapted to the inelastic case in comparison with the error estimator of Duflot and Bordas [49].

In the present paper is proposed an extension of these approaches combining X-FEM and automatic adaptive hierarchical mesh refinement dedicated to 2D and 3D crack propagation in elastic-plastic media. Considering a history-dependent material makes this extension not straightforward because remeshing implies field transfer which can be a delicate matter [11, 10, 12, 13], and usual techniques have to be adapted to X-FEM. Considering the X-FEM kinematics, there is no need to mesh the crack. Hence, the automatic adaptive mesh refinement strategy adopted can be the robust subdivision approach. The coupling between these two methods in the context of crack propagation modeling in a non-linear media is the main contribution of this work. The following sections first present the problem statement, then detail the numerical method developed (X-FEM, automatic AMR and field transfer) in sections 3, 4 and 5 and finally illustrate its efficiency and robustness on several 2D and 3D numerical applications. Even if this paper focuses on fatigue, the numerical methods aim at being employed for other kinds of fracture (brittle, ductile, creep...) with nonlinear material laws.

2. Problem statement

2.1. Mechanical problem

Let Ω be an open set of $\mathbb{R}^3$ denoting the domain of a solid deformable body containing a crack Γ. The boundary of Ω is named $\partial\Omega$ and can be split into $\partial\Omega_u$ on which apply Dirichlet boundary conditions and $\partial\Omega_F$ subjected to Neumann boundary conditions (3).

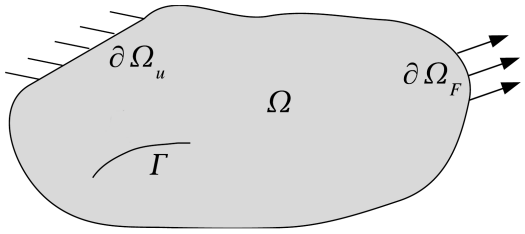

Figure 3: Mechanical model

The displacement field is noted $\boldsymbol{u}(\boldsymbol{x})$ and is considered sufficiently small so that assumptions of infinitesimal displacements, rotations and strains can be considered. Hence the linear stress tensor $\boldsymbol{\sigma}$ and the linearized strain tensor $\boldsymbol{\epsilon}$ can be adopted:

$$\boldsymbol{\epsilon} = \boldsymbol{\nabla}^s \boldsymbol{u} \tag{1}$$

The solution of this problem must satisfy both the static equilibrium characterized by the equation:

$$\boldsymbol{div}(\boldsymbol{\sigma}) = \boldsymbol{0} \text{ in } \Omega \tag{2}$$

and the boundary conditions:

$$\begin{cases} \boldsymbol{\sigma} \cdot \boldsymbol{n} = \boldsymbol{F}^{ext} \text{ on } \partial\Omega_F \\ \boldsymbol{u} = \boldsymbol{u}^{ext} \text{ on } \partial\Omega_u \end{cases} \tag{3}$$

In the present paper, non-linearity is limited to the constitutive law of the material. For instance, for an elastic-plastic behavior with the following decomposition into an elastic and a plastic part holds:

$$\boldsymbol{\epsilon} = \boldsymbol{\epsilon}^e + \boldsymbol{\epsilon}^p \tag{4}$$

and with the isotropic hardening constitutive laws:

$$\boldsymbol{\epsilon}^e = \boldsymbol{D}^{-1} : \boldsymbol{\sigma} \tag{5}$$

$$\phi(\boldsymbol{\sigma}, p) = \sigma_{vm}(\boldsymbol{\sigma}) - \sigma_Y(p) \leq 0 \tag{6}$$

$$\begin{cases} \text{if } \phi < 0 \quad \dot{\boldsymbol{\epsilon}}^p = 0 \\ \text{if } \phi = 0 \quad \dot{\boldsymbol{\epsilon}}^p = \lambda \frac{\partial \phi}{\partial \boldsymbol{\sigma}}\Big|_{p=cst} \text{ with } \lambda \geq 0 \end{cases} \tag{7}$$

$\boldsymbol{D}$ is the Hooke tensor, $\sigma_{vm} = ||\boldsymbol{\sigma} - \frac{1}{3} tr(\boldsymbol{\sigma}) \boldsymbol{I}||$ is the equivalent von Mises stress, $p = \int_{t_0}^{t} ||\dot{\boldsymbol{\epsilon}}^p|| dt$ is the equivalent plastic strain, ϕ is the yield function, σ_Y is the threshold stress whose dependence with the equivalent plastic strain is a characteristic of the material (i.e. the traction curve) and λ is the plastic multiplier.

2.2. Crack propagation

To achieve the description of the mechanical model, possibility for the crack to propagate has to be taken into account. Thus the crack surface Γ becomes time dependent and an evolution law has to be added to the model. However, when failure by fatigue is under consideration the discontinuity evolves slowly. Thus N, the number of loading cycles can be considered as a pseudo time variable. In 2D, this dependency can be parametrized by the propagation direction θ and the propagation velocity $\frac{da}{dN}$ where a is the crack length. Here a propagation criteria based on the stress intensity factors K_I and K_{II} is chosen.

The propagation direction is computed with equation (8) issued from [50] based on the maximal circumferential stress :

$$\theta = 2\, tan^{-1} \left(\frac{K_I}{K_{II}} - sgn(K_{II}) \sqrt{\left(\frac{K_I}{K_{II}}\right)^2 + 8} \right) \tag{8}$$

The propagation velocity can be computed using the well known Paris evolution law [51] or Elber evolution law [5]:

$$\frac{da}{dN} = C \left(\Delta K_{eq}\right)^m \tag{9}$$

where K_{eq} is a function of K_I and K_{II}. Neither the physical relevance of this criteria, nor its numerical computation are discussed here. But it must be noted that this criteria implies confined plasticity, which means that the zone around the crack front where plasticity occurs should remain limited (a limit value of $\frac{r_p}{a}$ around a few percent according to the literature [5], r_p being the radius of the plastic zone). In the applications test cases presented in sections 6.1 and 6.2 this hypothesis is not exactly verified, particularly at the end of the propagation. However the predicted crack path and crack velocity remains rather accurate.

When crack propagates, the configuration changes and, as a feedback effect, the mechanical equilibrium may also change. Since the times scales of the loading cycles and the crack propagation are separated it is relevant to adopt an uncoupled approach.

For a given mechanical loading and a given crack length, mechanical equilibrium is computed. Then,

once the equilibrium is reached, the propagation criteria is applied, giving a new crack length (or a number of cycles if crack increment is imposed).

This uncoupling between the time scale of the evolution of the mechanical loading and the time scale of crack propagation enables a direct and efficient procedure of crack propagation detailed in algorithm 1.

Algorithm 1: Iterative propagation algorithm using X-FEM and automatic adaptive mesh refinement.

- Initial healthy geometry and initial crack
- Boundary conditions and loading

repeat

- Refinement around the crack tip.
- Level-set creation on the new mesh using the old crack position
- Model and material on the refined mesh
- Enrichment of the relevant elements
- Field transfer on the new mesh
- Level-set and enrichment update using the new position of the crack
- Balancing step
- Mechanical computation
- Evaluation of a propagation criteria
- Step forward of the crack

until *End of propagation*;

- Post processing

On the one hand, the structure is meshed with quadrangular relatively coarse elements disregarding the existence of a crack. And on the other hand, the initial crack is meshed explicitly with a rather fine discretization. Boundary conditions and loading are defined on that geometry.

Then at each propagation step, the bulk mesh is refined around the crack front to obtain a suitable accuracy of the discretization in the area of interest. The details of this refinement will be developed in §4. Let $\mathcal{M}^{n+1}$ be that refined mesh for the propagation step $n+1$.

A finite element model is created on this refined mesh, using the material behavior presented in section 2.1. Using level-sets functions, an appropriate set of elements around the crack are enriched to allow crack opening. At first this enrichment considered the previous position of the crack. This enriched model will be presented in section §3.

Since the behavior of the structure is time dependent, it is then necessary to initialize the mechanical computation of a propagation step with the mechanical state of the structure at the end of the previous step. To do so, a field transfer procedure from $\mathcal{M}^n$ to $\mathcal{M}^{n+1}$ is needed. This operation must be realized with some precautions such as developed in section §5.

Once the previous state as been transfered on the new mesh, the model is updated with new enrichments to allow the crack opening toward the new position of the crack front. A non-linear solver enables to reach the equilibrium during a loading cycle and update the strain, stress and internal variables.

From the solution of this computation a propagation criterion is applied and crack growth is performed by adding a new layer of interfacial elements to the crack surface extending from the crack front.

From this new crack mesh the previous steps: refinement, model creation and enrichment, field transfer, mechanical computation, propagation criterion are repeated until the end of propagation is detected.

3. The eXtended Finite Element Method

3.1. Description of the crack

One main feature of the X-FEM is its ability to describe the crack geometry independently of the mesh of the structure. An explicit/implicit approach was implemented in Cast3M [52] very similar to the one concomitantly published by Fries [53]. It enables to combine advantages of both descriptions.

As a first step, the crack geometry is meshed with flat triangles in 3D (and with linear segment in 2D) independently of the structural mesh as depicted on figure 4a. It is the *explicit* description of the crack. It is worthwhile to notice that this mesh can be the support of local crack behavior like cohesive zone model [54] or frictional contact [40, 55].

As a second step, the level set functions named (ψ, ϕ) are computed at nodes of the structure close to the crack surface as illustrated on figure 4b. Those level stets allow an implicit geometric description of the crack [27, 56]. This step implies minimization of basic geometric computations which can be run in parallel since each nodal value is independent of the other.

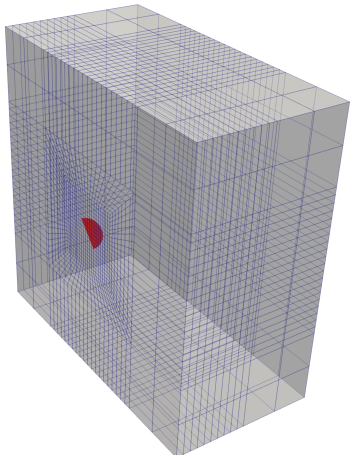

(a) Explicit description of the crack dissociated from the structural mesh

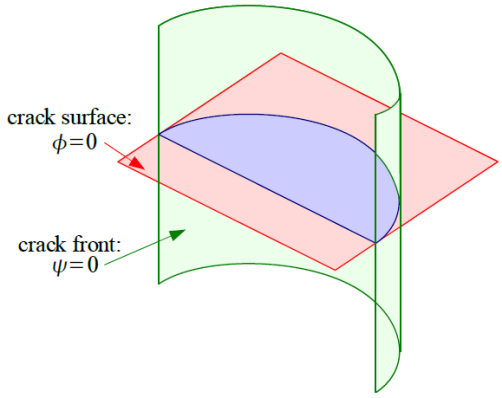

(b) Implicit description of the crack using level sets

Figure 4: Explicit/implicit description of the crack: example of a penny-shaped crack

3.2. Enrichment strategy

Once the crack is described by level set functions, it is then possible to enrich the displacement field by adding enrichment shape functions and the associated degrees of freedom to the discretization. Indeed, the mesh of the structure is built disregarding the crack, and the X-FEM enables to take it into account just by adding specific enrichment functions. With the help of partition of unity, discontinuous shape function defined by equation (10) is added at the nodes of the elements totally split by the crack, and the four singular shape functions of equation (11) are added at the nodes of the elements containing the crack front.

$$H(\boldsymbol{x}) = \begin{cases} +1 & \text{if } \phi(\boldsymbol{x}) > 0 \\ -1 & \text{if } \phi(\boldsymbol{x}) < 0 \end{cases} \tag{10}$$

$$\begin{aligned} F_1(\boldsymbol{x}) &= \sqrt{r}\,\sin(\theta/2) \\ F_2(\boldsymbol{x}) &= \sqrt{r}\,\sin(\theta/2)\sin(\theta) \\ F_3(\boldsymbol{x}) &= \sqrt{r}\,\cos(\theta/2) \\ F_4(\boldsymbol{x}) &= \sqrt{r}\,\cos(\theta/2)\sin(\theta) \end{aligned} \tag{11}$$

r and θ are polar coordinates of the point $\boldsymbol{x}$ in a local system of axes linked to the crack front as illustrated in figure 5. These local coordinates are deduced from the level-set functions like in [28, 27].

Let Ω_F denotes the nodes of the elements containing the crack front and Ω_H the nodes of the elements totally split by the crack. Then the X-FEM discretization of the displacement field can be defined by the equation (12):

$$\begin{aligned} \boldsymbol{u}(\boldsymbol{x},t) \simeq & \sum_{i\in\Omega} \boldsymbol{N}_i(\boldsymbol{x})\boldsymbol{u}_i(t) + \sum_{i\in\Omega_H} \boldsymbol{N}_i(\boldsymbol{x})H(\boldsymbol{x})\boldsymbol{a}_i(t) \\ & + \sum_{i\in\Omega_F} \boldsymbol{N}_i(\boldsymbol{x})\Big(\sum_{j=1..4} F_j(\boldsymbol{x})\boldsymbol{b}_{j,i}(t)\Big) \end{aligned} \tag{12}$$

where N_i is the finite element shape function associated to the node i of coordinate $\boldsymbol{x}_i$ of the mesh, and $\boldsymbol{u}_i$, $\boldsymbol{a}_i$ and $\boldsymbol{b}_{ij}$ are coefficients associated with the classical, discontinuous and singular degrees of freedom [25].

The singular enrichment function proposed by equation (11) are designed to fit the asymptotic behavior of the linear elastic fracture mechanic problem. As long as the behavior of the structure is elastic this enrichment function improves a lot the accuracy of the approximation since the shape functions fit exactly the expected singularity. When dealing with plasticity or elastodynamic problem, the expected singularity changes, so that the enrichment functions (11) are not the optimal ones. However those shape functions remain a good compromise between accuracy and efficiency for implementation in an industrial code. This enables the crack opening along the lips in the front element, which is a main feature of XFEM.

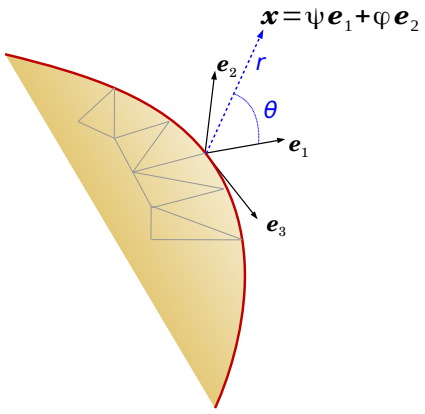

Figure 5: Level set functions determined for nearby points $\boldsymbol{x}$ of the structure in the local plane $(\boldsymbol{e}_1, \boldsymbol{e}_2)$.

For the sake of simplicity and to limit the number of degrees of freedom added in the discretization, a topological enrichment is chosen as illustrated

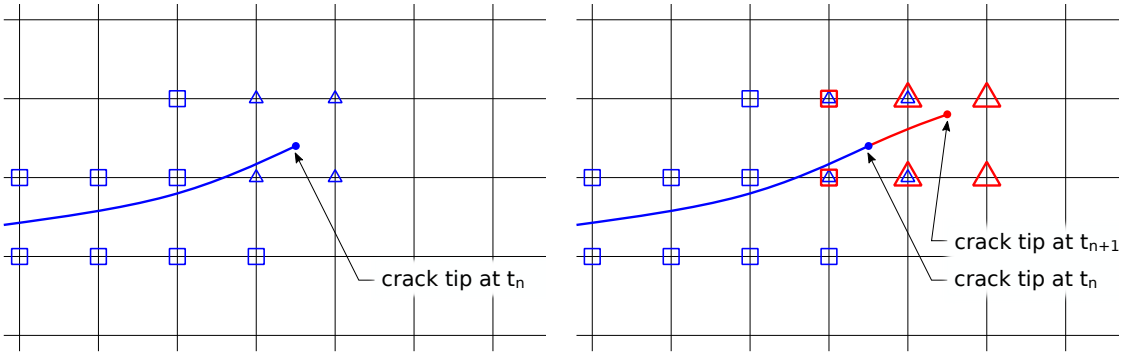

(a) Enrichment at time t_n (b) Enrichment at time t_{n+1}

Figure 6: Enrichment strategy

on figure 6. Only one layer on element around the crack is enriched. If the geometrical enrichment, in which a fixed zone aroud the crack tip is enriched, is known to have stronger convergence properties [57], this method can lead to a deterioration in the conditioning of the resulting stiffness matrix. An other strategy that could have been considered is the degrees of freedom gathering that has been introduced by Laborde *et al* [58] and extended to 3D by Agathos *et al* [59].

When crack propagates, new discontinuous and new singular degrees of freedom are added to the finite element approximation(marked by □ and △ on Figure 6b).

Consequently $\Omega_H(t_n)$ and $\Omega_F(t_n)$ are respectively included in $\Omega_H(t_{n+1})$ and $\Omega_F(t_{n+1})$. However the new F-functions are different from the previous ones taking into account the new position of the crack front. This strategy, initially proposed in [60], ensures energy conservation. However, if the crack grows relatively slowly in comparison to elements' size, the same set of nodes have a chance to be enriched with almost the same singular functions, leading to a bad conditioning of the elementary stiffness matrix. As a practical solution to avoid this case, it is proposed here to incrementally unenrich nodes which were previously enriched with singular functions from the previous time step. This can be easily achieved by identifying them and creating a kinematic constraint forcing them to zero at the end of the time step. In the example of figure 6b, this enrichment strategies implies that the "old" F-enriched nodes (i.e. marked by △) are the one which are imposed to zero during the time step from t_n to t_{n+1}.

3.3. Resolution of the discretized problem

The use of spatial approximation (12) does not change the nature of the system to be solved from the standard finite element method. In this example we use the Cast3M non linear solver [38]. The quasi-static equilibrium of equations (2) and (3) expressed in a weak form leads to the non linear discretized equation (13).

$$\boldsymbol{F}^{int}\big(\boldsymbol{u}(\boldsymbol{x},t_{n+1}),\boldsymbol{\sigma}(\boldsymbol{x},t_{n+1})\big) = \boldsymbol{F}^{ext}(t_{n+1}) \quad (13)$$

This equation is solved at every pseudo time step t_{n+1} of the loading cycle using the classical Newton-Raphson algorithm developed for example in [3]. Here the constitutive law is a non-linear isotropic hardening. The local resolution of the constitutive equation is tackled with a radial return algorithm. [61]

4. Automatic adaptive mesh refinement strategy

4.1. Hierarchic refinement

Since the X-FEM permits to mesh the structure ignoring the conformity with the crack, a simple mesh refinement procedure is possible in order to capture the different scales close to the crack tip with a locally relevant element size. The h-refinement [6] is adopted here. Its hierarchic nature is easy to implement and simplifies the field transfer step.

An important amount of literature exists about numerical implementation and performance of such approaches, so that they are not recalled here, as illustrated in figure 7. For brevity, given an initial coarse mesh $\mathcal{M}^n$ and a target density function h defined on this mesh, the refinement step consists in subdividing by power of 2^{dim} the elements whose the measured volume exceeds h^{dim} (dim$=2$ in 2D and $=3$ in 3D). This results in a new mesh named $\mathcal{M}^{n+1}$ and a set of linear relations to impose the continuity of the discretization at the hanging nodes of this new mesh. Those relations can be stored in a rectangular matrix γ as developed in the following paragraph.

The target density may be obtained with *a posteriori* error estimators like the Zienkiewicz and Zhu

one. Rodenas *et al* [62] have proposed an adaptation of the super convergence patch recovery method in the XFEM context to allow the use of this estimator. An other example of error estimator adapted to XFEM method is the one proposed by Duflot and Bordas [63, 49] relying on the moving least-squares smoothing and using the diffraction method to preserve the discontinuity.

However a simpler choice is made here by considering that the distance to the crack front characterizes the gradient of the solution, and then the need of fine mesh. In this work, the mesh refinement is not driven by an error indicator. The target density is *a priori* set as a function of the distance to the crack front as illustrated by figure 8. In XFEM context the distance to the crack front is simply $d = \sqrt{psi^2 + \phi^2}$. This approach avoids the pre-computation of a solution on a coarse mesh.

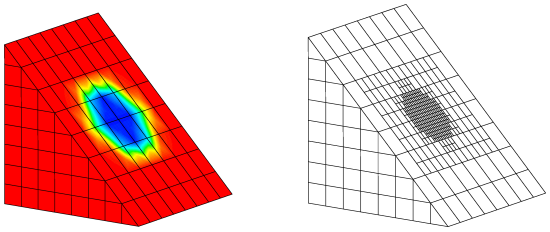

Figure 7: Target density on initial mesh and refined final mesh

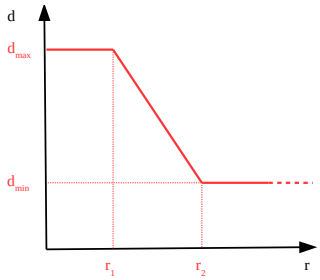

Figure 8: Target density as a fuction of the distance to the crack front.

4.2. *Management of the non-compatibility of the mesh*

As mentioned above, due to the non-compatibility of the refined mesh the continuity of the displacement field is not automatically fulfilled, contrary to finite element meshes. Fries [31] presents two different approaches to impose continuity on non-conformal meshes with X-FEM enrichment.

- The first consists in introducing a new partition of unity with specific shape functions for the elements with hanging nodes [64].
- In the second one, kinematic relations imposed with Lagrange multipliers (noted λ) allow to ensure continuity of the displacement field in a weak sense (mortar approximation [65]). This is the solution adopted in this work.

Lets consider that the hanging node k of coordinate x_k with the corresponding degree of freedom :

$$\boldsymbol{u}_k = \{\boldsymbol{e}_X \quad \boldsymbol{e}_Y \quad \boldsymbol{e}_Z\} \cdot \{u_{kX} \quad u_{kY} \quad u_{kZ}\}^T \quad (14)$$

Lets consider that this hanging node is the center of the non-compatible edge between nodes i and j (of coordinate x_i and x_j). Then continuity of the finite element approximation on both sides of the edge leads to the linear relation:

$$u_{kI} = \frac{1}{2}u_{iI} + \frac{1}{2}u_{jI} \quad (15)$$

for $I \in \{X, Y, Z\}$.

This is realized by introducing in the linear system a Lagrange multiplier λ_{kI}. The constraint (15) is then imposed in a weak form by:

$$\lambda^u_{kI}.\left(\frac{1}{2}u_{iI} + \frac{1}{2}u_{jI} - u_{kI}\right) = 0 \quad (16)$$

To maintain displacement continuity when some element have enriched nodes, the following rules have to be applied:

- *If a node (hanging or not) is involved in a compatibility relation and holds enriched degrees of freedom then the same compatibility relation must be imposed on the enriched degrees of freedom.*
- *Then the hanging node of this compatibility relation has to be a posteriori enriched (if it was not the case.)*

Hence the presence of hanging nodes in the enriched zone forces to: write compatibility relations for the enrichment degree of freedom, and add enrichment to some nodes which were not initially detected by the enrichment procedure.

For the first item above, thanks to the partition of unity, the continuity of the approximation can be written directly introducing a new Lagrange multiplier for the enrichment:

$$\lambda^a_{k\,I}.\left(\frac{1}{2}a_{i\,I} + \frac{1}{2}a_{j\,I} - a_{k\,I}\right) = 0 \quad (17)$$

for $I \in \{X, Y, Z\}$.

Figure 9 illustrates some specific situations where the second item cited above applies.

Adding those constraints to the discrete equilibrium resulting from the finite element model, $\boldsymbol{A}\boldsymbol{u} = \boldsymbol{b}$, leads classically to the following linear system:

$$\begin{bmatrix} \boldsymbol{A} & \boldsymbol{\gamma}^u_{kI} & \boldsymbol{\gamma}^a_{kI} \\ \boldsymbol{\gamma}^{u\,T}_{kI} & 0 & 0 \\ \boldsymbol{\gamma}^{a\,T}_{kI} & 0 & 0 \end{bmatrix} . \begin{bmatrix} \boldsymbol{u} \\ \lambda^u_{kI} \\ \lambda^a_{kI} \end{bmatrix} = \begin{bmatrix} \boldsymbol{b} \\ 0 \\ 0 \end{bmatrix} \quad (18)$$

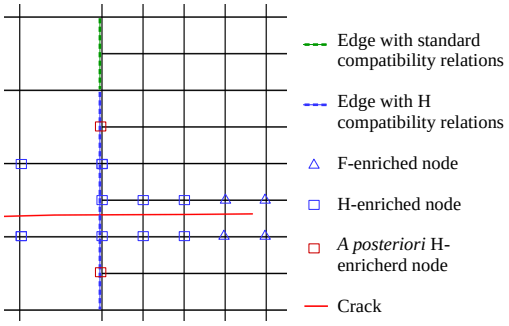

Figure 9: Enrichment strategy with incompatible meshes

γ^u_{kI} being a zero vector with -1 at positions ${}^u_{k\,I}$ and $1/2$ at position ${}^u_{i\,I}$ and ${}^u_{j\,I}$.

This constraint must be applied for each degree of freedom, I, of each hanging node, k, hence there is as many relations (and new Lagrange multipliers) as hanging nodes times the dimension of the problem. In practice the linear system (18) is always invertible, due to Dirichlet Boundary conditions and specific numerical solver accounting for redundant linear equations in Cast3M [66].

At this point coupling between X-FEM and automatic AMR is properly realized, but, in the context of history-dependent materials, a suitable field transfer strategy is needed.

5. Field transfer

5.1. General remarks

Based on an incremental approach of crack propagation with possible non-linear material, a new step of computation may start with a new crack position, from a given state of the structure.

Mapping (or transfer) from the previous discretization $\mathcal{M}^n$ to the new one $\mathcal{M}^{n+1}$ is needed for the displacement, strain, stress, and internal variables.

In the X-FEM and automatic AMR coupling context, not only the mesh but also the enrichment evolve. This is due to the crack growth, meaning that both aspects of the discretization change. This explains why this step must be done carefully. As already mentioned in the introduction, there exists several recipes [9, 11, 10, 12, 13] but few have been applied to X-FEM/G-FEM approaches.

In the present work the quantities elected to be transfered are: the stress tensor, the internal variables (e.g. the equivalent plastic strain) and the (enriched) displacement field. The other ones are deduced after projection steps. Taking advantage of the hierarchical nature of the local refinement, the following general procedure is adopted here:

1. Enrich the new mesh with the old position of the crack.
2. Transfer the displacement field (with enriched degrees of freedom) to the new mesh.
3. Transfer the stress and the internal variable fields to the integration points of the new mesh.
4. Set to zero every negative values of the internal variable.
5. Update the enrichment with the new position of the crack.
6. Perform a balancing step to recover the equilibrium and yield condition.

Step 2, 3 and 6 of this algorithm are detailed in the subsequent paragraphs.

5.2. Field transfer performed at the integration points

The difficulty lies in the fact that the field to transfer are only defined at the Gauss points thus there is no continuous approximation of them in the whole domain. A first approach proposed here is quite close to the one of Peric [10], Lee [11] or Mediavilla[12], but thanks to the hierarchical nature of the remeshing, it is simplified. This approach, that will be referred to as "naive" projection, is summarized by algorithm 2. First, the element, E^n, of the "old" mesh $\mathcal{M}^n$ where lies the "new" integration point, $\boldsymbol{x}_i^{n+1}$ is detected and its local coordinates computed. Then, the field under consideration is extrapolated from the "old" integration points to the nodes of this element. No averaging with the neighboring elements is done. A nodal vector $\hat{\boldsymbol{\sigma}}^n$ is obtained from the values, σ_n, known at the integration points of $\mathcal{M}^n$ by solving the equation (19). Finally finite element interpolation is performed to evaluate a value at each Gauss points in the element of the "new" mesh $\mathcal{M}^{n+1}$.

Remarks : This procedure can be done independently for every elements of the "old" mesh $\mathcal{M}^n$. This allows the procedure to be parallelized. Moreover,this limits the possible numerical diffusion during the projection. Indeed no information coming from the neighboring "old" elements is used to compute the projected values. So numerical errors can not be diffused by the projection beyond the size of one "old" element. However, a "naive" projection using only the classical shape function N leads to strong error when transferring variables like the equivalent plastic strain or the stress tensor.

As an illustration a mode I loading on a 2D square containing a crack is considered. A projection of a stress field $\boldsymbol{\sigma^n}$ obtained from an elasto-plastic computation is realized. This original field is plotted on figure 10a. The field is transfered using the projection procedure presented in algorithm 2 on the very mesh it is defined on, this example is called self-projection. Then the projection can be compared

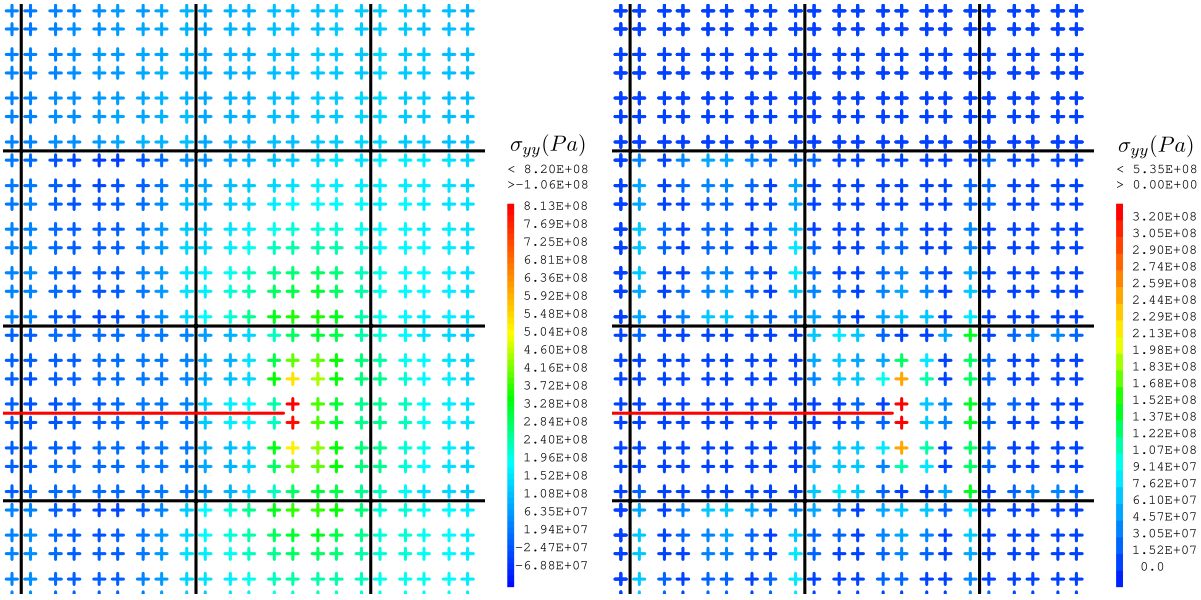

(a) Initial field $\boldsymbol{\sigma}^n$

(b) $|\boldsymbol{\sigma}^{n+1} - \boldsymbol{\sigma}^n|$ for "naive" projection

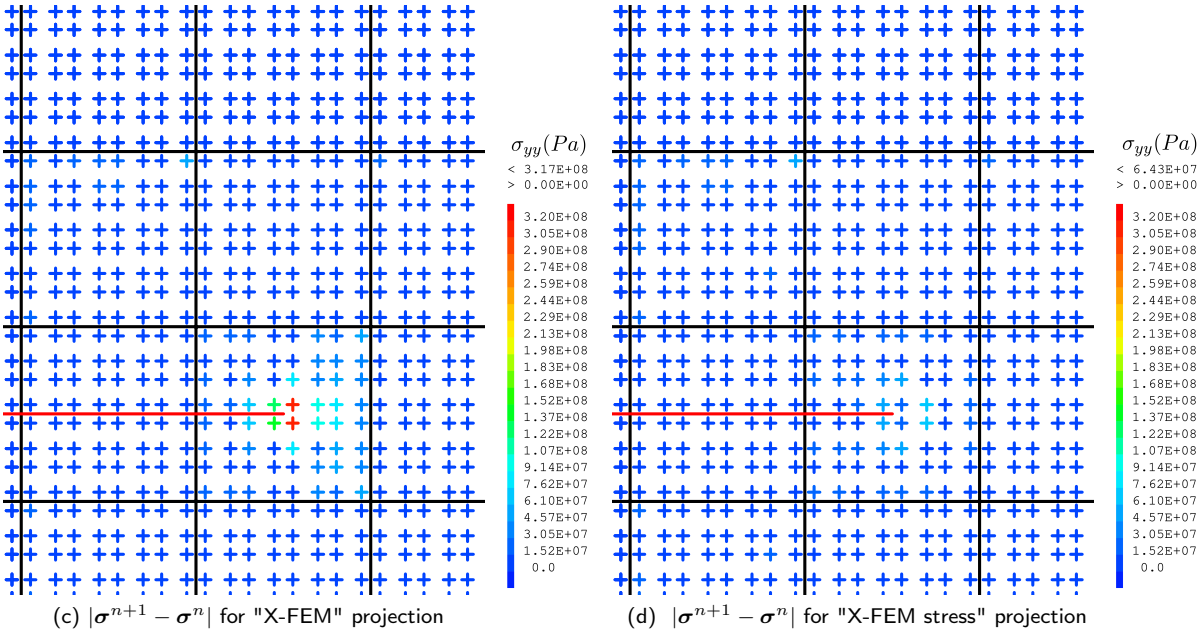

(c) $|\boldsymbol{\sigma}^{n+1} - \boldsymbol{\sigma}^n|$ for "X-FEM" projection

(d) $|\boldsymbol{\sigma}^{n+1} - \boldsymbol{\sigma}^n|$ for "X-FEM stress" projection

Figure 10: Stresses self-projection

Algorithm 2: Projection of σ from $\mathcal{M}^n$ integration points to $\mathcal{M}^{n+1}$ integration points

- For each integration points, $\boldsymbol{x}_i^{n+1}$ of $\mathcal{M}^{n+1}$, find the element, E^n of $\mathcal{M}^n$ where it lies and compute its local coordinates.

- A nodal vector $\hat{\boldsymbol{\sigma}}^n$ is extrapolated from the values of σ at $\mathcal{M}^n$ integration points, by solving the equation (19).

$$\int_{E^n} \boldsymbol{N}^{n^T}(\boldsymbol{x})\boldsymbol{N}^n(\boldsymbol{x})\hat{\boldsymbol{\sigma}}^n d\Omega = \int_{E^n} \boldsymbol{N}^{n^T}(\boldsymbol{x})\sigma^n(\boldsymbol{x})d\Omega \tag{19}$$

where $\boldsymbol{N}^n(\boldsymbol{x})$ is the vector of the standard shape functions in the element$E$ of mesh $\mathcal{M}^n$

- Evaluate the finite element interpolation at each integration point $\boldsymbol{x}_i^{n+1}$ of $\mathcal{M}^{n+1}$

$$\sigma^{n+1}(x_i^{n+1}) = \boldsymbol{N}^n(\boldsymbol{x}_i^{n+1})\hat{\boldsymbol{\sigma}}^n \tag{20}$$

to the original field at each integration points. figure 10b , 10c, and 10d, show the difference between the original field and the transfered one for tree different transfer methods. As we can see on figure 10b the "naive" self-projection induce a is rather significant error.

One of the main contributions of the present work is to remark that the "naive" projection presented above is not sufficient and that the X-FEM approximation must be used for extrapolation and interpolation. Indeed, a way to reduce the projection error is to include the enriched shapes function of the X-FEM formulation in the extrapolation and interpolation steps of the projection. The approach will be called "X-FEM" projection. and is described in details in algorithm 3. As illustrated on figure 10c the projection error is mainly limited to the vicinity of the crack tip but stays locally significant.

This error was expected since the enriched shapes functions of the X-FEM formulation are designed to represent the displacement field and not the strains or stress field. Indeed, if the discretized space generated by the derivatives of the classical finite element shape functions is included in the space generated by shape functions themselves, that is not the case for the X-FEM shape functions.

Thus a third approach that will be referred to as "X-FEM stress" projection is proposed. The idea is to enrich the finite element basis of shape functions with singular functions inspired from (11) but adapted to the representation of stresses, F_i^S defined by equation (24). Then use this enriched discretization in the projection procedure is described by equations (21), (22) and (23).

Algorithm 3: Projection of σ from $\mathcal{M}^n$ integration points to $\mathcal{M}^{n+1}$ integration points

- For each integration points,$\boldsymbol{x}_i^{n+1}$ of $\mathcal{M}^{n+1}$, find the element, E^n of $\mathcal{M}^n$ where it lies and compute its local coordinates.

- A vector $\hat{\boldsymbol{\sigma}}^n$ of size $6\,n_{no}$ is extrapolated from the values of σ at $\mathcal{M}^n$ integration points, by solving the equation (21).

$$\int_{E^n} \boldsymbol{\phi}^{n^T}(\boldsymbol{x})\boldsymbol{\phi}^n\hat{\boldsymbol{\sigma}}^n(\boldsymbol{x})d\Omega = \int_{E^n} \boldsymbol{\phi}^{n^T}(\boldsymbol{x}).\sigma^n(\boldsymbol{x})d\Omega \tag{21}$$

where $\boldsymbol{\phi}^n$ is an element vector of size $6\,n_{no}$ defined by equation (22):

$$\begin{cases} \boldsymbol{\phi}^n_{6(i-1)+1}(\boldsymbol{x}) = N_i^n(\boldsymbol{x}) \\ \boldsymbol{\phi}^n_{6(i-1)+2}(\boldsymbol{x}) = H(\boldsymbol{x})N_i^n(\boldsymbol{x}) \\ \boldsymbol{\phi}^n_{6(i-1)+3}(\boldsymbol{x}) = F_1(\boldsymbol{x})N_i^n(\boldsymbol{x}) \\ \boldsymbol{\phi}^n_{6(i-1)+4}(\boldsymbol{x}) = F_2(\boldsymbol{x})N_i^n(\boldsymbol{x}) \\ \boldsymbol{\phi}^n_{6(i-1)+5}(\boldsymbol{x}) = F_3(\boldsymbol{x})N_i^n(\boldsymbol{x}) \\ \boldsymbol{\phi}^n_{6(i-1)+6}(\boldsymbol{x}) = F_4(\boldsymbol{x})N_i^n(\boldsymbol{x}) \end{cases} \tag{22}$$

and n_{no} the number of nodes in element E^n.

- Evaluate the enriched finite element interpolation at each integration point $\boldsymbol{x}_i^{n+1}$ of $\mathcal{M}^{n+1}$

$$\boldsymbol{\sigma}^{n+1}(\boldsymbol{x}_i^{n+1}) = \boldsymbol{\phi}^n(\boldsymbol{x}_i^{n+1})\hat{\boldsymbol{\sigma}}^n \tag{23}$$

$$\begin{aligned} F_1^S(\boldsymbol{x}) &= \tfrac{1}{\sqrt{r}}\sin(\theta/2) \\ F_2^S(\boldsymbol{x}) &= \tfrac{1}{\sqrt{r}}\sin(\theta/2)\sin(\theta) \\ F_3^S(\boldsymbol{x}) &= \tfrac{1}{\sqrt{r}}\cos(\theta/2) \\ F_4^S(\boldsymbol{x}) &= \tfrac{1}{\sqrt{r}}\cos(\theta/2)\sin(\theta) \end{aligned} \tag{24}$$

Figure 10d shows that this approach leads to smaller error in this simple self-projection case.

Considering a basis of enrichment with all the derivatives of the enriched shape functions for the projection lead to near singular matrix $\boldsymbol{\phi}^{n^T}\boldsymbol{\phi}^n$ and rises difficulties in the resolution of equation (21). This justifies the use of the reduced basis (24) that includes the most important contribution to the stresses near the crack tip (proportional to $\frac{1}{\sqrt{r}}$).

In figure 11 the evolution of the error in terms of energy norm (defined by equation (25)) for the self-projection example with homogeneous h-refinement is showed. These evolution confirm the previous conclusion.

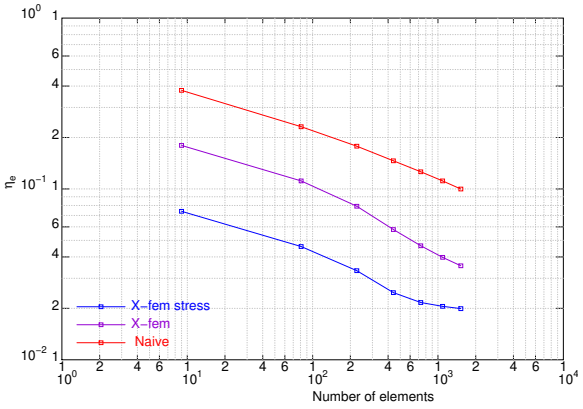

Figure 11: Error convergence of the stresses auto-projection example

$$\eta_e = \sqrt{\frac{\int_\Omega (\boldsymbol{\sigma}^n - \boldsymbol{\sigma}^{n+1}) : \boldsymbol{D^{-1}} : (\boldsymbol{\sigma}^n - \boldsymbol{\sigma}^{n+1})\, d\Omega}{\int_\Omega \boldsymbol{\sigma}^n : \boldsymbol{D^{-1}} : \boldsymbol{\sigma}^n\, d\Omega}} \tag{25}$$

5.3. Field transfer performed at the X-FEM nodes

Nodal field projection is an easy task when $\mathcal{M}^{n+1}$ is thinner than $\mathcal{M}^n$. In other words when the subspace of degrees of freedom $\mathbb{S}^n$ is included in $\mathbb{S}^{n+1}$. However, when $\mathcal{M}^{n+1}$ is locally coarser than $\mathcal{M}^n$ (un-refinement), some difficulties can arise, as illustrated in figure 13. In this example, a standard node i (of coordinate $\boldsymbol{x}_i$) in $\mathcal{M}^n$ becomes H-enriched in $\mathcal{M}^{n+1}$. Then the information contained in the u_i^n degree of freedom must be "distributed" between the standard one u_i^{n+1} and the enriched one a_i^{n+1}. This problem is locally ill-posed. So it not possible to transfer separately the standard degrees of freedom and the enriched ones. To avoid this difficulty of non compatible discretization spaces, the strategy described by algorithm 4 have been adopted and validated.

From the displacement field defined at the nodes of $\mathcal{M}^n$, a strain value at the integration points is obtained using matrix $\boldsymbol{B^n}$, containing the derivatives of the shapes functions of $\mathcal{M}^n$. This strain field is transfered to $\mathcal{M}^{n+1}$ using the "X-FEM stress" projection presented above, then integrated using a virtual linear problem. The displacement $\boldsymbol{u}^{n+1}$ is obtained by solving a virtual elastic equilibrium.

Figure 14 shows the convergence of the error in term of L_2 norm for a self-projection test. The L_2 error is defined as follows :

$$\eta_{L2} = \sqrt{\frac{\int_\Omega (\boldsymbol{u}^n - \boldsymbol{u^{n+1}}) \,.\, (\boldsymbol{u^n} - \boldsymbol{u^{n+1}}) d\Omega}{\int_\Omega (\boldsymbol{u}^n \,.\, \boldsymbol{u}^n)\, d\Omega}} \tag{30}$$

This error is computed with homogeneous h-refinement

Algorithm 4: Projection from $\mathcal{M}^n$ nodes to $\mathcal{M}^{n+1}$ nodes

- From the initial displacement $\boldsymbol{u}^n$, the strain $\boldsymbol{\epsilon}^n$ is computed at the integration points of the initial discretization, $\mathcal{M}^n$.

$$\boldsymbol{\epsilon}^n = \boldsymbol{B}^n \boldsymbol{u}^n = \boldsymbol{\nabla}^s \boldsymbol{u}^n \tag{26}$$

- Strain $\boldsymbol{\epsilon}^n$ is projected onto the final configuration $\boldsymbol{\epsilon}^{n+1}$ using the "X-FEM stress" projection.

- A virtual linear stress is computed form that stain.

$$\boldsymbol{\sigma}_{line}^{n+1} = \boldsymbol{D}\boldsymbol{\epsilon}^{n+1} \tag{27}$$

- The corresponding nodal forces $\boldsymbol{F}^{\text{int}^{n+1}}$ are evaluated

$$\boldsymbol{F}^{\text{int}^{n+1}} = \int_{\mathcal{M}^{n+1}} \boldsymbol{B}^{n+1^T} \boldsymbol{\sigma}_{line}^{n+1} d\Omega \tag{28}$$

- The linear system is solved then $\boldsymbol{u}^n + 1$ is obtained as the projection of $\boldsymbol{u}^n$

$$\int_{\mathcal{M}^{n+1}} \boldsymbol{B}^{n+1^T} \boldsymbol{D} \boldsymbol{B}^{n+1}\, d\Omega\, \boldsymbol{u}^{n+1} = \boldsymbol{F}^{\text{int}^{n+1}} \tag{29}$$

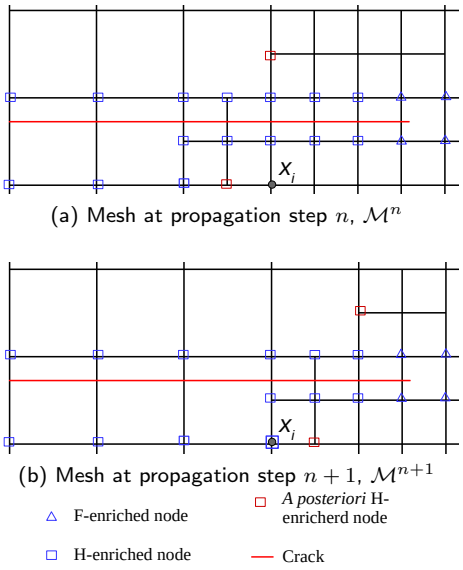

(a) Mesh at propagation step n, $\mathcal{M}^n$

(b) Mesh at propagation step $n+1$, $\mathcal{M}^{n+1}$

Figure 12: Example of incompatible discretization

and the projection procedure of algorithm 4. As expected, since there is an auto-projection error for the stresses with algorithm 3 (as shown on figure 11) there is also an auto-projection error for the displacement in the approach proposed here but this error converges with the size of the elements.

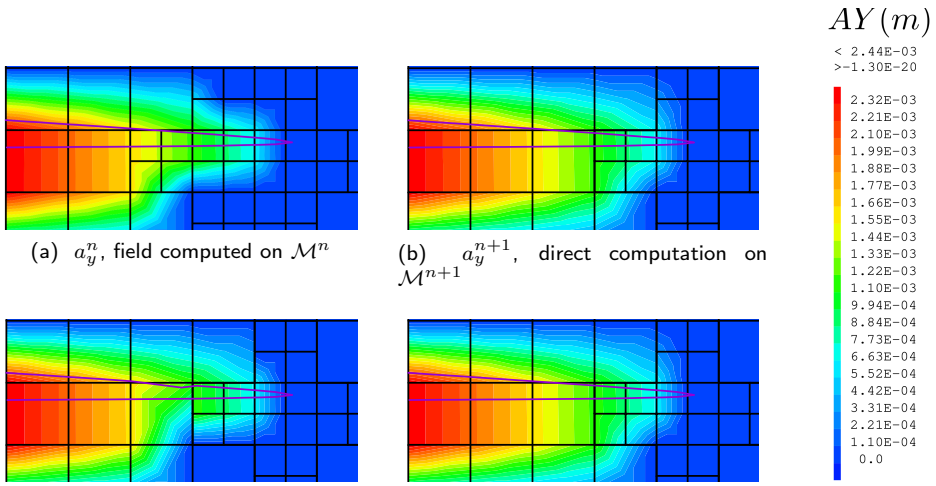

(a) a_y^n, field computed on $\mathcal{M}^n$

(b) a_y^{n+1}, direct computation on $\mathcal{M}^{n+1}$

(c) a_y^{n+1}, projection using the standard shape functions

(d) a_y^{n+1}, projection using algorithm 4

Figure 13: Projection of the 'AY' degree of freedom

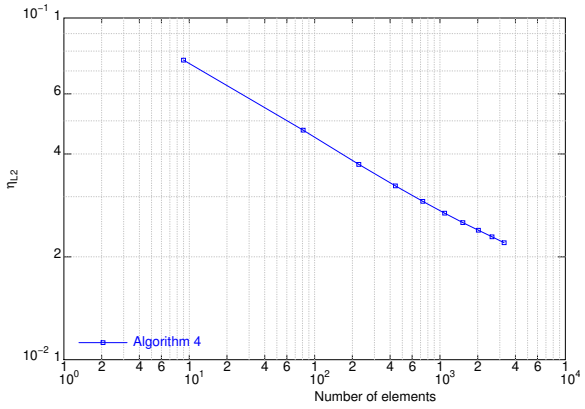

Figure 14: Convergence with the auto-projection displacement field

Figure 13 shows the interest of this approach in the situation of incompatible discretization. Figure 13a shows the field of the a_y^n degrees of freedom representing the mode I crack opening in an elastic media computed on the enriched mesh $\mathcal{M}^n$, defined on figure 12a. Figure 13b shows the same field for the same loading but computed on mesh $\mathcal{M}^{n+1}$ defined on figure 12b. On figures 13c and 13d, the a_y field issued form tow different projection of a_y^n (computed on $\mathcal{M}^n$) on $\mathcal{M}^{n+1}$ are plotted. As this problem is elastic, the projected fields should be exactly the same as the direct computation of figure 13b. The projection used to obtain figure 13c field has been done by directly evaluating the finite element approximation of $\mathcal{M}^n$ at the nodes of $\mathcal{M}^{n+1}$. Figure 13c show that this "standard" projection is not able to provide the right value of a_y at the node X_i for which the two discretization are incompatible. On the contrary, the projection of algorithm 4 gives a correct projected a_y^{n+1} field, as illustrated on figure 13d.

5.4. *Balancing step*

Once the fields are transfered on the new discretization we proceed to a balancing step to recover an admissible state in agreement with governing equations (2), (5), (6) and (7) as suggested in [12].

6. Illustration of the method on numerical applications

6.1. *Example of 2D elastic-plastic crack propagation problem*

In this section our methodology for crack propagation is used to simulate a bi-dimensional mixed mode propagation test that has been performed by Rethoré *et al.* Our numerical results are compared to the experimental ones obtained in [67].

A thin plate is considered with the following dimensions: length $L = 150$ mm , width $l = 50$ mm and thickness $e = 4$ mm. This plate is pierced with a $d = 5$ mm diameter hole in its center and a notch of initial length $a_0 = 5$ mm is created on one edge of the plate with a variable offset from the center of the hole $\delta \in \{2.5\,\text{mm}, 4\,\text{mm}, 6\,\text{mm}\}$ as illustrated on figure 16. This offset will be a parameter of this study. This plate is made of 316L steel. It is modeled with an isotropic hardening elastic-plastic behavior. The material properties of 316L steel are the following :

- Young modulus : $E = 208.182\,GPa$
- Poisson ratio : $\nu = 0.3$

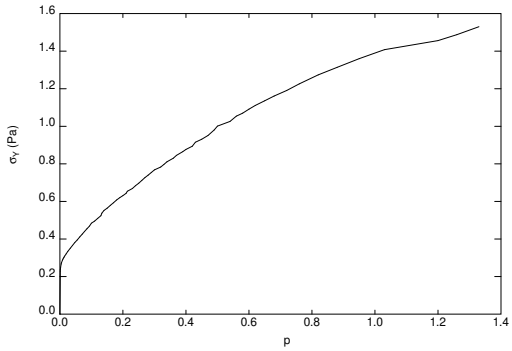

Figure 15: Tensile test, yield strength (Pa) against the equivalent strain for steel 316L

- Experimental stress-strain curves has been established with a 1D tensile test as illustrated on figure 15.

In 2D, the vertical displacement of the plate lower edge L_{inf} is blocked, and the upper edge L_{sup} is summited to cyclic fatigue loading. These cycles are applied with a $5\,Hz$ frequency and a ratio $F_{min}/F_{max} = 0.1$. Two different levels of maximum loading are considered on different specimens:

$F_{max} \in \{15\,\text{kN},\ 22.5\,\text{kN}\}$.

The loading frequency is low enough to neglect the inertia effects. Thus we can use a quasi-static model.

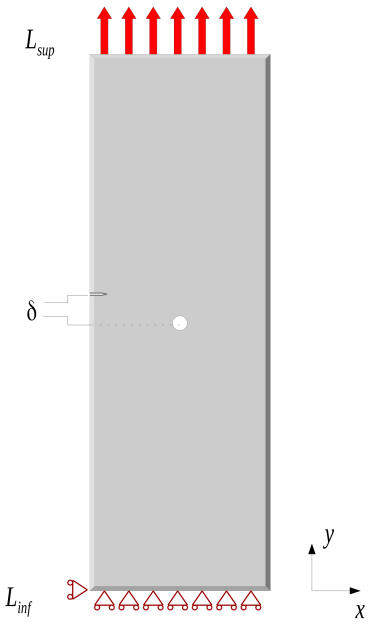

Figure 16: Precracked plate with a hole

This fatigue test has been simulated in 2D using the procedure presented here, refining the mesh only around the crack. Between each propagation step a 0.25 mm long crack increment of is added in the direction computed by equation (8).

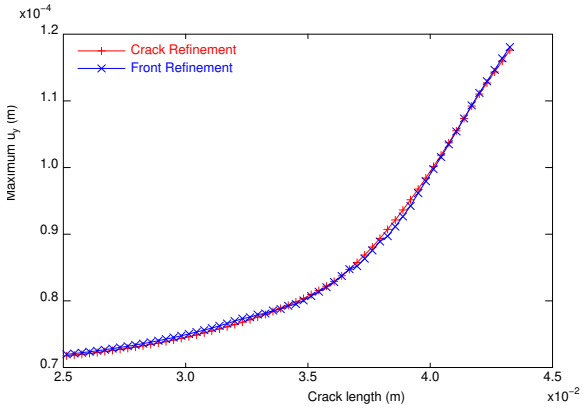

Figure 17: Global response of the cracked plate for the two refinement strategy

Good agreement can be observed between the simulation and the experimentation in term of crack path. The crack is first loaded mainly in mode I and so propagates in a straight line. Then, closer to the hole, the dis-symmetry of the loading induce the crack turns in direction on the hole. For the first 2 positions of the offset $\delta \in \{2.5\text{ mm}, 4\text{ mm}\}$ the crack dives into the hole whereas for $\delta = 6$ mm the crack approaches the hole but eventually continues in the horizontal direction as illustrated on figure 18.

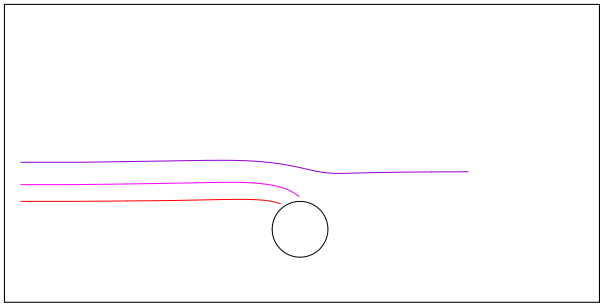

Figure 18: Simulated crack path for $\delta \in \{2.5$ mm, 4 mm, 6 mm$\}$

The computation has been done for two different refinement strategies: refining all along the crack as illustrated on figure 19a and refining only around the crack front and coarsening after it as illustrated on figure 19b. In the two cases residual stresses in a plastic wake along the crack path are visible. Of course in the second strategy the mesh is coarsened along the crack away from the crack tip. So this plastic wake is not well discretized. However the use of the enriched base of approximation for the projection allows discontinuities in that coarse zone. In figure 17 the maximal vertical displacement of fatigue cycle is plotted against the crack length during the propagation for the two refinement strategies. We can see that if the local shape of the plastic wake is affected

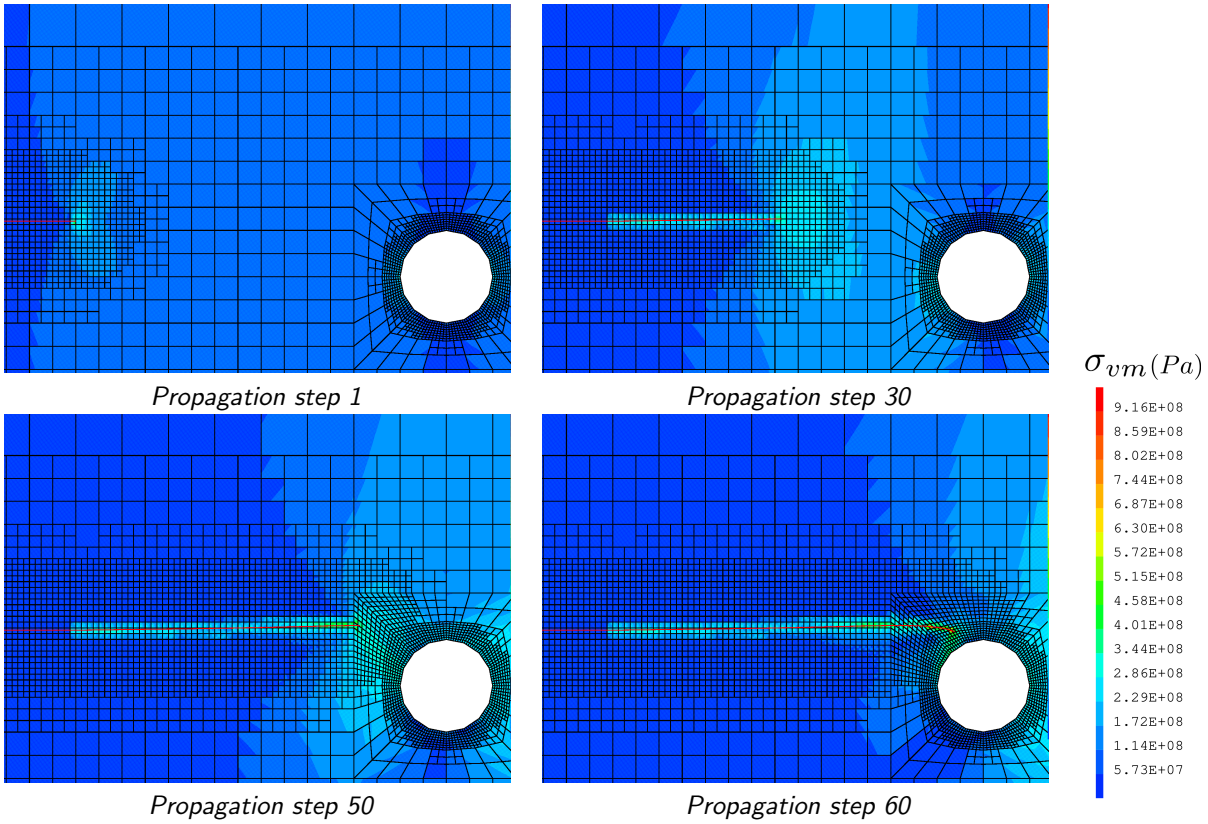

(a) Crack refinement

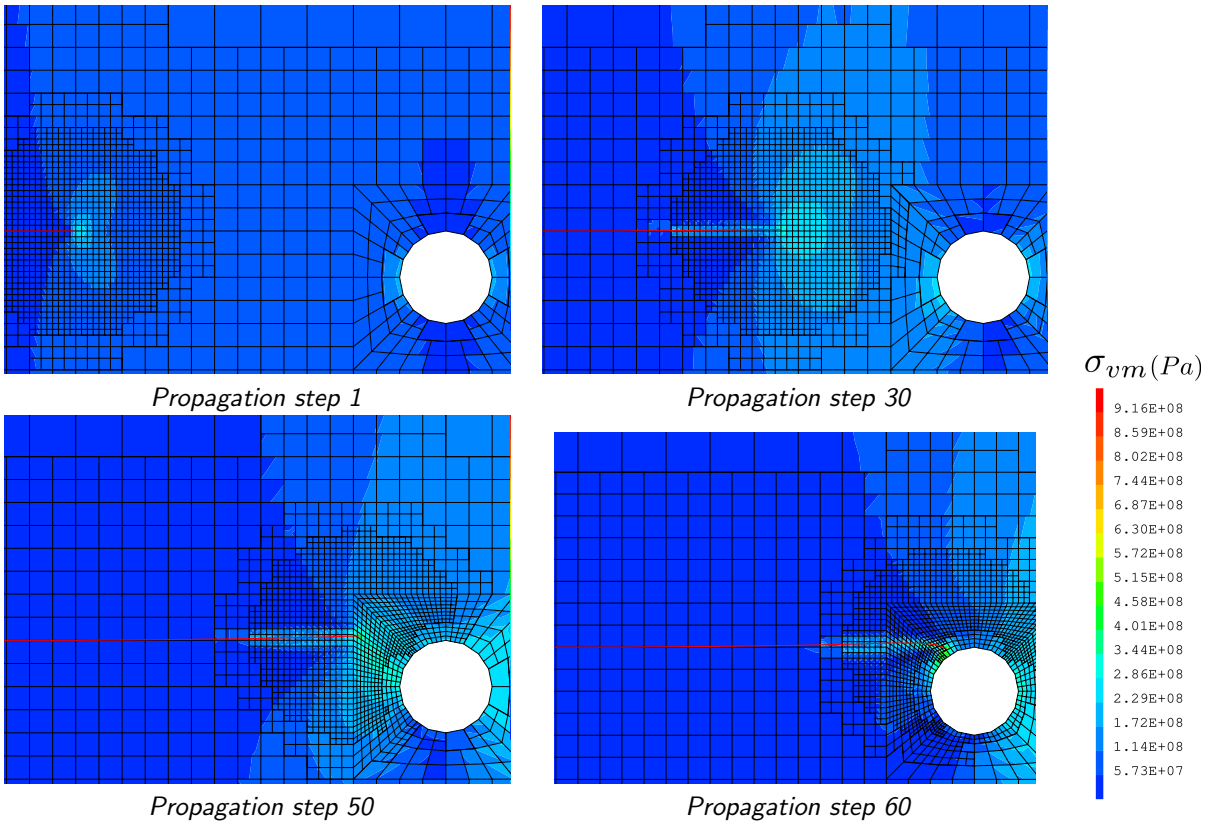

(b) Front refinement

Figure 19: von Mises stresses during mixed mode propagation $F_{max} = 15\,\text{kN}$, $\delta = 2,5\,\text{mm}$

by the coarsening, the global response of the sample is not.

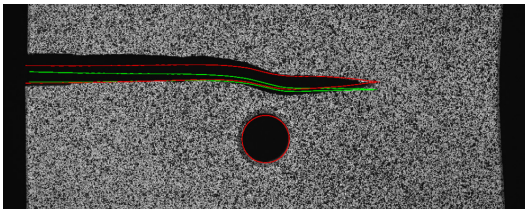

Figure 20: Elastic simulation in green, Elastic-plastic simulation in red $Fmax = 22.5$ kN, $\delta = 6$ mm

In figure 20 the experimental picture of the deformed plate during propagation is superposed with the lip of the crack computed form the X-FEM modelization with an elastic and an elastic-plastic model. In this particular case ($\delta = 6$ mm, $F_{max} = 22,5$ kN) plasticity has an important influence on the crack opening. The elastic-plastic modelization proposed here leads to an acceptable agreement with the experimental observation with limited number of elements : 5119 on the last mesh. This agreement could be improved by a better modelization of the boundary conditions of this test but this is beyond the scope of this paper.

6.2. Simulation of 3D compact tension sample

In this section a compact tension sample has been meshed in 3D using the presented propagation procedure: the mesh is refined around the crack front as illustrated on figure 22a or all along the crack surface as illustrated on figure 22b. The dimensions of the sample are the following: length 62.5 mm , width 60 mm and thickness 12.5 mm. For this example the 304L industrial steel is considered and its material characteristics are the following:

- Young modulus : $E = 329.9$ GPa
- Poisson ratio : $\nu = 0.3$
- The experimental stress-strain curve has been established with a 1D tensile test as illustrated on figure 21.
- The Paris Law coefficients have been established experimentally by Gourdin *et al* [68] : $\frac{da}{dN} = 1.406 \times 10^{-}9(\Delta K_{eq})^{3.299}$ with $\frac{da}{dN}$ in mm/cycles and ΔK_{eq} in MPa$\sqrt{\text{m}}$

The sample is loaded with a fatigue cycle with an imposed strength on pins.

In the literature one can find several 3D propagation criteria, Richard lists and compare a significant number of them in in [69]. However, the study of those 3D propagation criteria and the numerical methods to implement them is not the objective of this paper. So, in this simple example, the crack front is considered as a straight line and the 2D propagation criteria presented in § 2.1 is used. Between each propagation step a 0.25 mm long crack increment is added in the direction computed by equation (8) The number of load cycles correspnding to this crack increment is computed using equation (9).

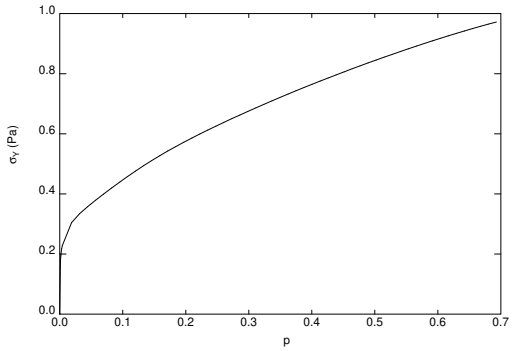

Figure 21: Tensil test: yield strength (Pa) against the equivalent strain for steel 304L

Due to the symmetry of the problem only a quarter of the sample needs to be simulated. Specific boundary conditions must be applied on the two planes of symmetry in particular in the plane $y = 0$ which is the plane of the crack. The following conditions must be applied on the elements adjacent to this plane:

$$\begin{aligned} \boldsymbol{u}_x(y) &= \boldsymbol{u}_x(-y) \\ \boldsymbol{u}_y(y) &= -\boldsymbol{u}_y(-y) \\ \boldsymbol{u}_z(y) &= \boldsymbol{u}_z(-y) \end{aligned} \tag{31}$$

Given the enrichment strategy described by (12) and parity of those enrichment functions, the boundary condition of equation (31) is met by imposing on the crack plan ($y = 0$):

$$\begin{cases} a_x = b_{x1} = b_{x4} = 0 \\ a_z = b_{z1} = b_{z4} = 0 \\ u_y = b_{y3} = b_{y2} = 0 \end{cases} \tag{32}$$

Figure 23 shows the displacement and its enriched component representing the crack opening during the propagation for a mesh only refined around the crack front. On figure 24 the crack opening at the maximal load of a fatigue cycle is plotted against the crack length during the propagation for a simulation with coarsening (Front refinement), a simulation without coarsening (Crack refinement) and compared to experimental data that was obtained in the CEA [68]. We can see that the global response of the sample is not affected by the coarsening. Indeed the agreement between experimental data and simulation is the same for the two discretization. On the other hand the computational cost of the front refinement strategy is much lower. Table 1 shows the average

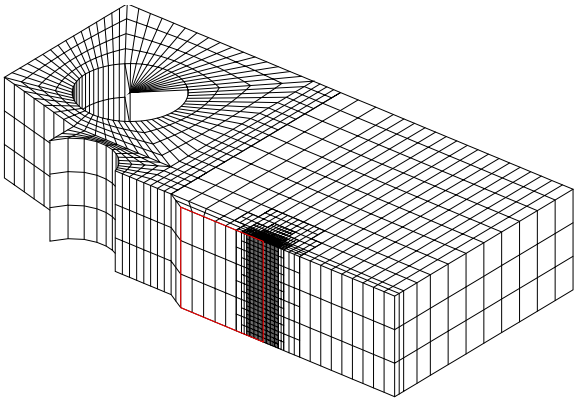

(a) refinement around the crack front

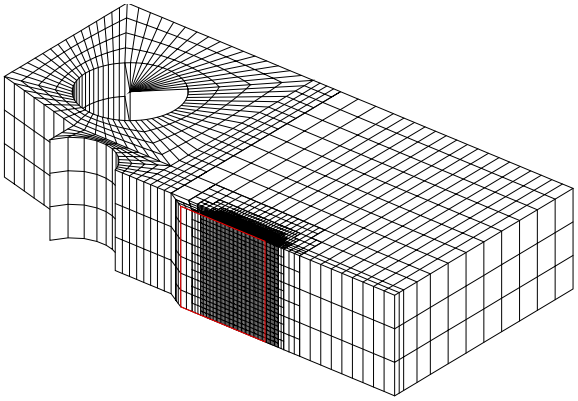

(b) refinement along the crack surface

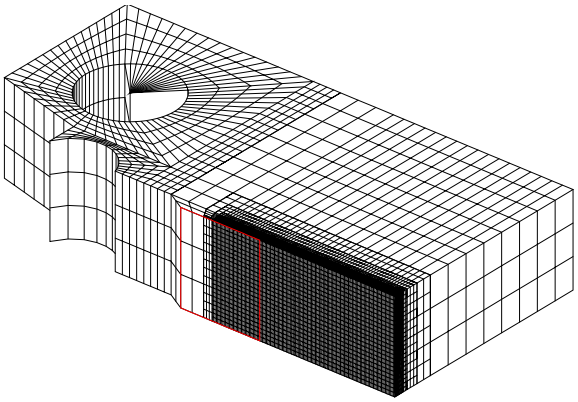

(c) non adaptive refinement around the crack path

Figure 22: Meshes at the propagation step 25 for different refinement strategies

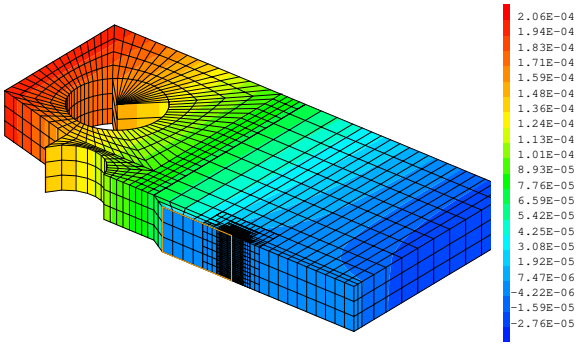

(a) Vertical displacement, u_y (m)

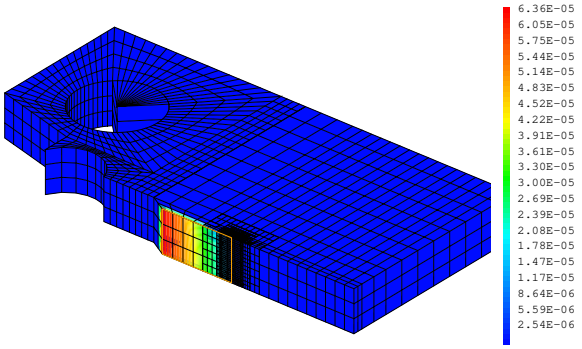

(b) Crack opening, a_y (m)

Figure 23: Displacement and crack opening on the 3D sample. Propagation step : 25 Front refinement

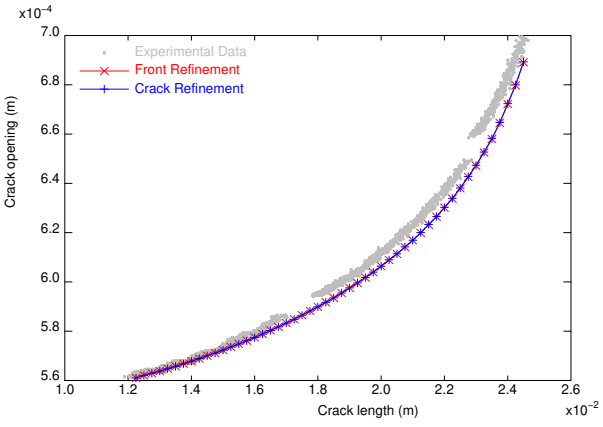

Figure 24: Crack opening against the crack length for the two different refinement strategies compare to experimental data

number of elements in the meshes used during the propagation for the two refinement strategies proposed here and for a non-adaptive strategy in which all the zone the where crack could propagate is refined.

Non-adaptive refinement	Crack refinement	Front refinement
68395	26362	11238

Table 1: Average number of elements during the propagation for different refinement strategies

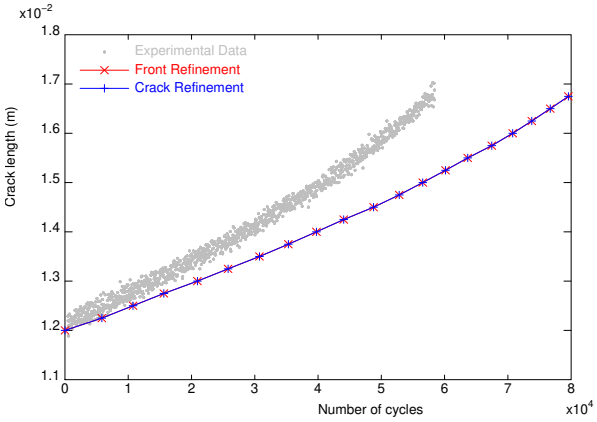

Figure 25: Crack opening against the crack length for the two different refinement strategies compare to experimental data

Figure 25 shows the crack length plotted against the number of load cycles for both refinement strategies and during the experimentation. The agreement between the simulated and the computed crack velocity is not quite satisfying. To improve it a 3D propagation criteria and a curved representation of the crack front might be needed.

7. Conclusion

The objective of this work is to provide an efficient and robust procedure to simulate 3D elastic-plastic crack propagation without *a priori* knowlege of the crack path. To do so, a multi scale approach coupling the X-FEM method with automatic adaptive mesh refinement has been presented in this paper.This approach is close to Fries one [31] for elastic problems. But, in the context of history dependent behavior a projection of the mechanical state from one mesh to another during the propagation is necessary. The handling of this projection step is the main contribution of the present paper. For quantities only defined at the integration points, as well as for the nodal displacement field new transfer procedures have been proposed to tackle the difficulty risen by the evolution of the enrichment from one mesh to another.

The quality of this transfer procedure has been evaluated for 2D elastic-plastic simple examples. Then the method has been applied in 2D and 3D cases where the simulation results could be compared to experimental data. These results show the robustness and adaptability of the procedure providing highly accurate results for a modest computational cost compared to the alternative of uniform refinement.

This propagation procedure has been applied here to quasi-static examples of fatigue crack propagation. However the robustness of the modeling allows to extend the applications to many different cracking problems given the relevant propagation criteria. For instance, the extension to dynamic cracking is under consideration. The introduction of a damage model or cohesive laws could also be done with minor impact to the procedure.

Another promising prospect is the choice of an error estimator to control and optimize the mesh adaptation procedure.

References

[1] A. A. Griffith, M. Eng, Vi. the phenomena of rupture and flow in solids, Phil. Trans. R. Soc. Lond. A 221 (582-593) (1921) 163–198.

[2] G. R. Irwin, Analysis of stresses and strains near the end of a crack traversing a plate, J. appl. Mech. 24 (3) (1957) 361–364.

[3] J. Chaboche, J. Lemaitre, A. Benallal, R. Desmorat, Mécanique des matériaux solides, Dunod, Paris, 2009.

[4] M. F. Kanninen, C. L. Popelar, Advanced fracture mechanics, Oxford University Press, 1985.

[5] T. Elguedj, Simulation numérique de la propagation de fissure en fatigue par la méthode des éléments finis étendus : prise en compte de la plasticité et du contact-frottement, Ph.D. thesis, Institut National des Sciences Appliquées de Lyon (2006).

[6] O. C. Zienkiewicz, J. D. S. Gago, D. W. Kelly, The hierarchical concept in finite element analysis, Computers & Structures 16 (1-4) (1983) 53–65.

[7] O. Zienkiewicz, R. Taylor, J. Zhu, The Finite Element Method: Its Basis And Fundamentals, 6th Edition, Butterworth-Heinemann, 2005.

[8] A. Berard, Transferts de champs entre maillages de type éléments finis et applications numériques en mécanique non linéaire des structures, Ph.D. thesis, Université de Franche-Comté (2011).

[9] M. Ortiz, J. Quigley Iv, Adaptive mesh refinement in strain localization problems, Computer Methods in Applied Mechanics and Engineering 90 (1-3) (1991) 781–804.

[10] D. Perić, C. Hochard, M. Dutko, D. R. J. Owen, Transfer operators for evolving meshes in small strain elasto-placticity, Computer Methods in Applied Mechanics and Engineering 137 (3-4) (1996) 331–344.

[11] N.-S. Lee, K.-J. Bathe, Error indicators and adaptive remeshing in large deformation finite element analysis, Finite Elements in Analysis and Design 16 (2) (1994) 99–139.

[12] J. Mediavilla, R. Peerlings, M. Geers, A robust and consistent remeshing-transfer operator for ductile fracture simulations, Computers & structures 84 (8-9) (2006) 604–623.

[13] D. Brancherie, P. Villon, A. Ibrahimbegovic, On a consistent field transfer in non linear inelastic analysis and

ultimate load computation, Computational Mechanics 42 (2) (2008) 213–226.
[14] R. Branco, F. Antunes, J. Costa, A review on 3d-fe adaptive remeshing techniques for crack growth modelling, Engineering Fracture Mechanics.
[15] B. Carter, P. Wawrzynek, A. Ingraffea, Automated 3-d crack growth simulation, International journal for numerical methods in engineering 47 (1-3) (2000) 229–253.
[16] M. Schöllmann, M. Fulland, H. Richard, Development of a new software for adaptive crack growth simulations in 3d structures, Engineering Fracture Mechanics 70 (2) (2003) 249–268.
[17] D. V. Swenson, A. R. Ingraffea, Modeling mixed-mode dynamic crack propagation using finite elements: theory and applications, Computational Mechanics 3 (6) (1988) 381–397.
[18] V. Chiaruttini, D. Geoffroy, V. Riolo, M. Bonnet, An adaptive algorithm for cohesive zone model and arbitrary crack propagation, European Journal of Computational Mechanics 21 (3-6) (2012) 208–218.
[19] A. Khoei, M. Eghbalian, H. Moslemi, H. Azadi, Crack growth modeling via 3d automatic adaptive mesh refinement based on modified-spr technique, Applied Mathematical Modelling 37 (1) (2013) 357–383.
[20] K. Murotani, G. Yagawa, J. B. Choi, Adaptive finite elements using hierarchical mesh and its application to crack propagation analysis, Computer Methods in Applied Mechanics and Engineering 253 (2013) 1–14.
[21] K. Park, G. H. Paulino, W. Celes, R. Espinha, Adaptive mesh refinement and coarsening for cohesive zone modeling of dynamic fracture, International Journal for Numerical Methods in Engineering 92 (1) (2012) 1–35.
[22] A. Meyer, F. Rabold, M. Scherzer, Efficient finite element simulation of crack propagation using adaptive iterative solvers, International Journal for Numerical Methods in Biomedical Engineering 22 (2) (2006) 93–108.
[23] H. Badnava, M. A. Msekh, E. Etemadi, T. Rabczuk, An h-adaptive thermo-mechanical phase field model for fracture, Finite Elements in Analysis and Design 138 (2018) 31 – 47.
[24] R. Patil, B. Mishra, I. Singh, An adaptive multiscale phase field method for brittle fracture, Computer Methods in Applied Mechanics and Engineering 329 (2018) 254–288.
[25] T. Belytschko, T. Black, Elastic crack growth in finite elements with minimal remeshing, International Journal for Numerical Methods in Engineering 45 (5) (1999) 601–620.
[26] C. A. Duarte, I. Babuška, J. T. Oden, Generalized finite element methods for three-dimensional structural mechanics problems, Computers & Structures 77 (2) (2000) 215–232.
[27] A. Gravouil, N. Moës, T. Belytschko, Non planar 3d crack growth by the extended finite element and level sets part ii: Level set update, International Journal for Numerical Methods in Engineering 53 (11) (2002) 2569–2586.
[28] N. Moës, A. Gravouil, T. Belytschko, Non planar 3d crack growth by the extended finite element and level sets part i: Mechanical model, International Journal for Numerical Methods in Engineering 53 (11) (2002) 2549–2568.
[29] B. Karihaloo, Q. Xiao, Modelling of stationary and growing cracks in fe framework without remeshing: a state-of-the-art review, Computers & Structures 81 (3) (2003) 119–129.
[30] T. Belytschko, R. Gracie, G. Ventura, A review of extended/generalized finite element methods for material modeling, Modelling and Simulation in Materials Science and Engineering 17 (4) (2009) 043001.
[31] T. P. Fries, T. Belytschko, The extended/generalized finite element method: An overview of the method and its applications, Int. J. Numer. Meth. Engng. (2010) 253–304.
[32] M. Surendran, S. Natarajan, S. P. A. Bordas, G. S. Palani, Linear smoothed extended finite element method, International Journal for Numerical Methods in Engineering 112 (12) (2017) 1733–1749.
[33] S. P. Bordas, T. Rabczuk, N.-X. Hung, V. P. Nguyen, S. Natarajan, T. Bog, N. V. Hiep, et al., Strain smoothing in fem and xfem, Computers & structures 88 (23-24) (2010) 1419–1443.
[34] L. Chen, T. Rabczuk, S. P. A. Bordas, G. Liu, K. Zeng, P. Kerfriden, Extended finite element method with edge-based strain smoothing (esm-xfem) for linear elastic crack growth, Computer Methods in Applied Mechanics and Engineering 209 (2012) 250–265.
[35] S. Mousavi, N. Sukumar, Generalized Gaussian quadrature rules for discontinuities and crack singularities in the extended finite element method, Computer Methods in Applied Mechanics and Engineering 199 (49-52) (2010) 3237–3249.
[36] B. Paul, M. Ndeffo, P. Massin, N. Moës, An integration technique for 3d curved cracks and branched discontinuities within the extended finite element method, Finite Elements in Analysis and Design 123 (2017) 19–50.
[37] B. Prabel, A. Combescure, A. Gravouil, S. Marie, Level set x-fem non matching meshes: application to dynamic crack propagation in elastic-plastic media, International Journal for Numerical Methods in Engineering 69 (8) (2006) 1553–1569.
[38] Cast3M. Finite Element software developed by the french Atomic Energy Center (CEA), www-cast3m.cea.fr (2018).
[39] B. Prabel, S. Marie, A. Combescure, Using the x-fem method to model the dynamic propagation and arrest of cleavage cracks in ferritic steel, Engineering Fracture Mechanics 75 (10) (2008) 2984–3009.
[40] B. Trollé, Simulation multi-échelles de la propagation des fissures de fatigue dans les rails, Ph.D. thesis, Institut National des Sciences Appliquées de Lyon (2014).
[41] J. Rannou, A. Gravouil, M. C. Baïetto Dubourg, A local multigrid xfem strategy for 3d crack propagation, International Journal for Numerical Methods in Engineering 77 (4) (2009) 581–600.
[42] J. Rannou, Prise en compte d'effets d'échelle en mécanique de la rupture tridimmensionnelle par une approche x-fem multigrille localisée non-linéaire, Ph.D. thesis, Villeurbanne, INSA (2008).
[43] J. Passieux, J. Réthoré, A. Gravouil, M. Baietto, Local/global non-intrusive crack propagation simulation using a multigrid x-fem solver, Computational Mechanics 52 (6) (2013) 1381–1393.
[44] J. P. Pereira, C. A. Duarte, D. Guoy, X. Jiao, hp-generalized fem and crack surface representation for non-planar 3-d cracks, International Journal for Numerical Methods in Engineering 77 (5) (2009) 601–633.
[45] J. Pereira, C. A. Duarte, X. Jiao, Three-dimensional crack growth with hp-generalized finite element and face offsetting methods, Computational Mechanics 46 (3) (2010) 431–453.
[46] Y. Jin, O. González-Estrada, O. aard, S. Bordas, Error-controlled adaptive extended finite element method for 3d linear elastic crack propagation, Computer Methods in Applied Mechanics and Engineering 318 (2017) 319–348.
[47] T. P. Fries, A. Byfut, A. Alizada, K. W. Cheng, A. Schröder, Hanging nodes and xfem, Int. J. Numer. Meth. Engng. 86 (4-5) (2011) 404–430.
[48] C. Prange, S. Loehnert, P. Wriggers, Error estimation for crack simulations using the xfem, International Journal for Numerical Methods in Engineering 91 (13) (2012) 1459–1474.
[49] M. Duflot, S. Bordas, A posteriori error estimation for extended finite elements by an extended global recovery,

International Journal for Numerical Methods in Engineering 76 (8) (2008) 1123–1138.
[50] H. Tada, P. C. Paris, G. R. Irwin, The stress analysis of cracks handbook, Del Research Corporation, Hellertown, PA (1973) 1.
[51] P. Paris, F. Erdogan, A critical analysis of crack propagation laws, Journal of basic engineering 85 (4) (1963) 528–533.
[52] B. Prabel, T. Yuritzinn, T. Charras, A. Simatos, Propagation de fissures tridimensionnelles dans des matériaux inélastiques avec xfem dans cast3m, in: 10e colloque national en calcul des structures, 2011.
[53] T. P. Fries, M. Baydoun, Crack propagation with the extended finite element method and a hybrid explicit implicit crack description, International Journal for numerical methods in engineering 89 (12) (2012) 1527–1558.
[54] A. Simatos, B. Prabel, S. Marie, M. Nedelec, A. Combescure, Modelling the tearing crack growth in a ductile ferritic steel using x-fem elements, in: ASME 2011 Pressure Vessels and Piping Conference, American Society of Mechanical Engineers, 2011, pp. 281–294.
[55] E. Pierres, M.-C. Baietto, A. Gravouil, A two-scale extended finite element method for modelling 3d crack growth with interfacial contact, Computer Methods in Applied Mechanics and Engineering 199 (17-20) (2010) 1165–1177.
[56] N. Sukumar, D. Chopp, B. Moran, Extended finite element method and fast marching method for three-dimensional fatigue crack propagation, Engineering Fracture Mechanics 70 (1) (2003) 29–48.
[57] E. Béchet, H. Minnebo, N. Moës, B. Burgardt, Improved implementation and robustness study of the x fem for stress analysis around cracks, International Journal for Numerical Methods in Engineering 64 (8) (2005) 1033–1056.
[58] P. Laborde, J. Pommier, Y. Renard, M. Salaün, High-order extended finite element method for cracked domains, International Journal for Numerical Methods in Engineering 64 (3) (2005) 354–381.
[59] K. Agathos, E. Chatzi, S. P. Bordas, D. Talaslidis, A well-conditioned and optimally convergent xfem for 3d linear elastic fracture, International Journal for Numerical Methods in Engineering 105 (9) (2016) 643–677.
[60] J. Réthoré, A. Gravouil, A. Combescure, An energy-conserving scheme for dynamic crack growth using the extended finite element method, International Journal for Numerical Methods in Engineering 63 (5) (2005) 631–659.
[61] T. Belytschko, W. K. Liu, B. Moran, K. Elkhodary, Nonlinear finite elements for continua and structures, John wiley & sons, 2013.
[62] J. J. Ródenas, O. A. González-Estrada, J. E. Tarancón, F. J. Fuenmayor, A recovery-type error estimator for the extended finite element method based on singular+ smooth stress field splitting, International Journal for Numerical Methods in Engineering 76 (4) (2008) 545–571.
[63] S. Bordas, M. Duflot, P. Le, A simple error estimator for extended finite elements, Communications in Numerical Methods in Engineering 24 (11) (2008) 961–971.
[64] A. K. Gupta, A finite element for transition from a fine to a coarse grid, International Journal for Numerical Methods in Engineering 12 (1) (1978) 35–45.
[65] R. de Borst, E. Ramm, Multiscale methods in computational mechanics: progress and accomplishments, Vol. 55, Springer Science & Business Media, 2010.
[66] V. Pierre, Notice d'utilisation cast3m reso, Tech. rep., CEA (2016).
[67] T. Quemin, E. Ivanovic, G. Baratte, M. Coret, J. Réthoré, Suivi par corrélation d´ images du benchmark fatacrack, in: 23 ème Congrès Français de Mécanique, 2017.
[68] C. Gourdin, G. Perez, P. Le Delliou, G. Leopold, Investigations on crack propagation under cyclical isothermal and thermo-mechanical loadings for a type 304-l stainless steel used for pressurized water reactor, MATEC Web of Conferences 165 (19004).
[69] H. Richard, M. Fulland, M. Sander, Theoretical crack path prediction, Fatigue & fracture of engineering materials & structures 28 (1-2) (2005) 3–12.